frontiers in Materials

ORIGINAL RESEARCH
published: 25 June 2021
doi: 10.3389/fmats.2021.651875

# Research on the Homogenized Postirradiation Elastoplastic Constitutive Relations for Composite Nuclear Fuels

*Jing Zhang[1], Jingyu Zhang[1], Haoyu Wang[2], Hongyang Wei[1,2], Changbing Tang[2], Chuan Lu[2], Shurong Ding[1]* and Yuanming Li[2]**

[1]Department of Aeronautics and Astronautics, Institute of Mechanics and Computational Engineering, Fudan University, Shanghai, China, [2]Science and Technology on Reactor System Design Technology Laboratory, Nuclear Power Institute of China, Chengdu, China

A multi-scale finite element method is developed to simulate the irradiation process and postirradiation uniaxial tensile tests for metal-matrix composite fuels with representative volume elements (RVEs). The simulations of irradiation process are implemented under a wide range of burnup levels, with the irradiation effects on the mechanical constitutive relations of fuel particles and matrix taken into account comprehensively. The simulation results for the macroscopic postirradiation true stress/strain curves are obtained, excluding the irradiation-induced macroscopic deformations. The effects of particle fission density, temperature, and initial particle volume fraction are investigated and analyzed. The research results indicate that 1) a quasi-elastic stage appears during the postirradiation tension, which is mainly induced by the creation of high residual compressive stresses in the particles and matrix after irradiation; 2) with the increase of effective strains, new plastic deformations increase in the particles and matrix to result in the macroscale plastic stage; 3) the macroscale irradiation softening and hardening phenomena appear, which mainly stem from the weakened deformation resistance by the irradiation-induced plastic deformations in the matrix, the enlarged particle volume fraction after irradiation, and the irradiation hardening effects of metal matrix.

**Keywords: metal-matrix composite fuel, postirradiation, residual stresses and strains, effective stress–strain curve, homogenization theory, multi-scale simulation**

OPEN ACCESS

***Edited by:***
*Fei Gao,*
*University of Michigan, United States*

***Reviewed by:***
*Ping Duan,*
*China University of Geosciences, China*
*Jianming Xue,*
*Peking University, China*

****Correspondence:***
*Shurong Ding*
*dingshurong@fudan.edu.cn*
*Yuanming Li*
*lym_npic@126.com*

***Specialty section:***
*This article was submitted to Structural Materials, a section of the journal Frontiers in Materials*

***Received:*** *11 January 2021*
***Accepted:*** *25 May 2021*
***Published:*** *25 June 2021*

***Citation:***
*Zhang J, Zhang J, Wang H, Wei H, Tang C, Lu C, Ding S and Li Y (2021) Research on the Homogenized Postirradiation Elastoplastic Constitutive Relations for Composite Nuclear Fuels. Front. Mater. 8:651875. doi: 10.3389/fmats.2021.651875*

## INTRODUCTION

Utilization of metal-matrix composite fuels in fast reactors and advanced nuclear systems (Vatulin et al., 2001; International Atomic Energy Agency, 2006; Lipkina et al., 2014; Aoki et al., 2019) has been considered as a means to depleting the inventories of plutonium and minor actinides in the spent fuels from commercial thermal reactors. With deep burnup (Neeft et al., 2003; Savchenko et al., 2006; Savchenko et al., 2009), the loaded radioactive materials can be disposed sufficiently. A composite of plutonium dioxide particles and the zircaloy matrix ($PuO_2$/Zr) is one of the metal-matrix fuel concepts (Duyn, 2003; Savchenko et al., 2007). These kinds of nuclear fuels have also been proposed for generation-IV reactors (Carmack et al., 2006; International Atomic Energy Agency, 2006; Lombardi et al., 2008) because of their high thermal conductivity and long service lifetime.

In order to calculate the in-pile thermomechanical behavior (Wang et al., 2010; Wang et al., 2011; Gong et al., 2014) in a full-sized fuel rod or fuel assembly with PuO2/Zr fuel pellets filled, the homogenized postirradiation elastoplastic property of this composite should be obtained. The irradiation tests and postirradiation uniaxial tensile tests should be performed. In the extreme irradiation environments of nuclear reactors, irradiation swelling of fuel particles increases with fission density as a result of continuous accumulation of solid and gaseous fission products (MacDonald and Thompson, 1978; Suzuki, 2005; Cui et al., 2015), which leads to the enhancement of the mechanical interactions between the particles and matrix, and causes the configuration variation of composite fuels (Rest, 1995; Kim et al., 2015). Besides, the particles and matrix experience elastoplastic deformations, induced by their mechanical interactions and external forces. It should be noted that plastic deformations are irreversible, and the subsequent mechanical constitutive relations depend on the accumulated equivalent plastic strains and loading paths (Chan and Lee, 1993; George, 2012). Thus, the achieved fission density has an effect on the postirradiation effective elastoplastic behavior of composite nuclear fuels if plastic deformations occur in the fuel particles and matrix during irradiation. What is more, the residual stresses have been proven to affect the mechanical properties of materials (Shi et al., 2017; Sun et al., 2020). It can be known that the residual stresses produced after irradiation also influence the postirradiation effective elastoplastic behavior. Simultaneously, the metal matrix undergoes irradiation hardening (Byun and Farrell, 2004; Jiang et al., 2011) and creep deformations (Rodriguez et al., 1984; Adamson and Coleman, 2019) owing to the in-pile attack of high-energy fission fragments and fast neutrons. These above irradiation effects need to be involved in simulation of the irradiation process, which will have influences on the postirradiation effective elastoplastic behavior.

The metal-matrix composite fuel of $PuO_2$/Zr is similar to that of particle reinforced composites (Ding et al., 2010; Wang et al., 2010; Wang et al., 2011), whose effective properties (Doghri and Friebel, 2005; Zhao et al., 2014; Liu et al., 2018) can be obtained with the homogenization theory–based multi-scale research method. The macroscopic mechanical response can be usually predicted *via* the volumetric averaging of the mesoscopic mechanical variables, that is, mean-field method, which has been demonstrated to be efficient for particle reinforced composite materials, laminated materials, fiber-reinforced composite materials, and so on (Nemat-Nasser, 1999; SemihPerdahcıoglu and Hubert, 2011). In this method, each phase is assumed to follow its own macroscopic thermal–mechanical behaviors. The mean-field theory for effective elastoplastic performances of composite materials has been developed over many years, and can be carried out with analytical methods (Voigt, 1889; Reuss, 1929; Eshelby, 1957; Budiansky and Wu, 1961; Hill, 1965; Mori and Tanaka, 1973; Lielens et al., 1998; Doghri et al., 2011; Abedini and Chen, 2014; Wu et al., 2015) and numerical simulation methods (Hill, 1963; Sun and Vaidya, 1996; Matsuda et al., 2002; Bouhamed et al., 2019; Samadian et al., 2020). There are some classical analytical models for effective elastic properties of composites, such as the upper and lower bounds for elastic modulus proposed by Voigt and Reuss (Voigt, 1889; Reuss, 1929), the Eshelby equivalent inclusion model (Eshelby, 1957), the self-consistent (SC) model (Budiansky and Wu, 1961; Hill, 1965), the Mori–Tanaka model (Mori and Tanaka, 1973), and the Lielens interpolation model (Lielens et al., 1998), among others. The linearization techniques have also been expanded to study plastic performances (Doghri et al., 2011; Abedini and Chen, 2014; Wu et al., 2015), including the secant-based approach and tangent-based approach. With the development of finite element techniques, direct finite element computations have been used to obtain the effective elastoplastic behavior of composites (Hill, 1963; Sun and Vaidya, 1996; Matsuda et al., 2002; Bouhamed et al., 2019; Samadian et al., 2020), through which the real microstructure of composite materials can be reflected. According to Hill theory (Hill, 1963), a representative volume element (RVE) should be selected to perform the finite element (FE) computation and homogenization process, and the appropriate boundary conditions to ensure periodicity need to be applied on the RVE. C. T. Sun et al. (Sun and Vaidya, 1996) established the RVE models for composites under different loading cases, and the obtained effective elastic constants matched well with the experimental data. They mentioned that this methodology could be extended to model the elastoplastic behavior of composites. Abir Bouhamed et al. (Bouhamed et al., 2019) numerically determined the effective elastoplastic property of Titanium Grade 2/Al-6061 composite. J. Y. Zhang et al. (Zhang and Ding, 2020) studied the homogenized elastoplastic behavior of FeCrAl alloys based on the mean-field method, and the results agree well with experimental results. It can be concluded that the macroscopic elastoplastic properties of composites can be acquired with the FE simulation of real tests combined with the mean-field theory. However, no work in the current literatures can be found to estimate the postirradiation effective elastoplastic properties of metal-matrix fuels.

In this study, a representative volume element model is established for the composite fuel of $PuO_2$/Zr, and a coupled process of irradiation and postirradiation uniaxial tensile tests is numerically implemented on the ABAQUS platform. The deformation contributions of matrix creep, particle creep, and swelling are all taken into account in simulations of irradiation tests. The influences of residual stresses are considered in the postirradiation uniaxial tensile tests. The postirradiation effective elastoplastic curves are obtained by the developed homogenization algorithm and procedures, which are verified through the designed simulation tests for the homogenization models and multiparticle models. Then, the influences of irradiation dose, test temperature, and initial particle volume fraction are investigated. The stress/strain contributions of matrix and particle to the homogenized performances are analyzed.

## FINITE ELEMENT MODELING

The finite element simulations of irradiation process and postirradiation uniaxial tensile tests for $PuO_2$/Zr fuels are carried out with the commercial software ABAQUS. The mechanical constitutive relations and the stress update algorithms for the fuel particles and matrix are defined with verified user-defined subroutines as those in our previous studies (Gong et al., 2014; Zhao et al., 2016). In this section, the irradiation-related material properties for the fuel particles and matrix are given, together with the established finite element model and the developed homogenization algorithm, to obtain the postirradiation effective stress–strain behavior.

## The Material Performance Models

1) for the fuel particles

The elastic strain increments for the fuel particles are calculated as

$$\Delta\varepsilon_{ij}^{e} = \Delta\varepsilon_{ij} - \Delta\varepsilon_{ij}^{sw} - \Delta\varepsilon_{ij}^{cr} - \Delta\varepsilon_{ij}^{p}, \tag{1}$$

where $\Delta\varepsilon_{ij}$ depicts the total strain increments, $\Delta\varepsilon_{ij}^{sw}$ represents the irradiation swelling strain increments, $\Delta\varepsilon_{ij}^{cr}$ denotes the irradiation creep strain increments, and $\Delta\varepsilon_{ij}^{p}$ describes the plastic strain increments. The models of elasticity constants, plasticity, and irradiation swelling explained in the study by Hill (1965), MacDonald and Thompson (1978), Rest (1997), Rest (2004), Suzuki (2005), Gong et al. (2014), Wu et al. (2015) are utilized.

### The Irradiation Swelling Model

It is noted that the irradiation swelling consists of the two contributions of solid swelling and gaseous swelling, which is validated in our recent study (Zhang et al., 2021) with the results of irradiation experiments.

The fission solid swelling is expressed as

$$\frac{\Delta V_{\text{solid}}}{V} = 2.5\times10^{-29}\cdot Fd, \tag{2}$$

where $V$ is the initial fuel volume in $m^3$, $Fd$ depicts the fission density in fissions/$m^3$, and $\Delta V_{\text{solid}}$ is the volume change caused by solid fission products in $m^3$.

A mechanistic model of fission gas swelling with the recrystallization effect taken into account can be described as (Rest, 1997; Rest, 2004)

$$\frac{\Delta V_{\text{gas}}}{V} = \begin{cases} (\Delta V_{\text{intra}}/V)|_{r_{gr}} + (\Delta V_{\text{inter}}/V)|_{r_{gr}} Fd \le Fd_x \\ (1-V)_r\left[(\Delta V_{\text{intra}}/V)|_{r_{gr}} + (\Delta V_{\text{inter}}/V)|_{r_{gr}}\right] \\ \quad + V_r\,(\Delta V_{\text{inter}}/V)|_{r_{grx}} Fd > Fd_x, \end{cases} \tag{3}$$

where the expressions of the intragranular bubble swelling $(\Delta V_{\text{intra}}/V)|_{r_{gr}}$, intergranular bubble swelling $(\Delta V_{\text{inter}}/V)|_{r_{gr}}$ before recrystallization, and intergranular bubble swelling at the recrystallization zone $(\Delta V_{\text{inter}}/V)|_{r_{grx}}$ can be found in the study by Abedini and Chen (2014), Wu et al. (2015). The fission rate–dependent critical fission density of $Fdx$ (Hill, 1965) can be described as $Fd_x = 4\times10^{24}(\dot{f})^{2/15}$, with $\dot{f}$ denoting the fission rate in fissions/($m^3$·s).

### The Irradiation Creep Model

The irradiation creep rate model is described as (MacDonald and Thompson, 1978)

$$\dot{\varepsilon}^{cr} = \frac{\left(A_1 + A_2\dot{f}\right)\sigma_1 \exp\left(-Q_1/RT\right)}{(A_3+D)G^2} + \frac{\left(A_4 + A_8\dot{f}\right)\sigma_2^{4.5}\exp\left(-Q_2/RT\right)}{A_6+D} + A_7\sigma\dot{f}\exp\left(-Q_3/RT\right)\ \ (s^{-1}), \tag{4}$$

where $A_1 = 0.3919$, $A_2 = 1.3100\times10^{-19}$, $A_3 = -87.7$, $A_4 = 2.0391\times10^{-25}$, $A_6 = -90.5$, $A_7 = 3.72264\times10^{-35}$, and $A_8 = 0.0$; the temperature of $T$ is in K, and the theoretical density of $D$ is considered as 95%; with the grain size $G = 7$ μm and the gas constant $R = 1.9872$ cal/(molK), the fission rate of $\dot{f}$ is in fissions/($m^3$•s); the von Mises stress of $\sigma$ is in Pa; when $\sigma \le 16547416.8/G^{0.5714}$, $\sigma_1 = \sigma$ and $\sigma_2 = 0.0$; when $\sigma > 16547416.8/G^{0.5714}$, $\sigma_1 = 16547416.8/G^{0.5714}$ and $\sigma_2 = \sigma$; and $Q_i$ denotes the activation energy in cal/mol, which is described in the study by MacDonald and Thompson (1978).

2) for the Zircaloy matrix

The elastic stain increments are calculated as

$$\Delta\varepsilon_{ij}^{e} = \Delta\varepsilon_{ij} - \Delta\varepsilon_{ij}^{cr} - \Delta\varepsilon_{ij}^{p}, \tag{5}$$

where $\Delta\varepsilon_{ij}$ represents the total strain increments, $\Delta\varepsilon_{ij}^{cr}$ denotes the creep strain increments, and $\Delta\varepsilon_{ij}^{p}$ depicts the plastic strain increments. The models of elasticity constants explained in the study by Hales et al. (2016) are adopted, which depend on the irradiation doses.

### Irradiation Creep and Thermal Creep Models

The considered creep rate model (Hayes and Kassner, 2006; Hales et al., 2016) includes the contributions of thermal creep and irradiation creep, given as

$$\dot{\varepsilon}_m^{cr} = \dot{\varepsilon}^{ss} + \dot{\varepsilon}^{ir}, \tag{6}$$

where $\dot{\varepsilon}^{ss}$ is the thermal creep strain rate in 1/s, expressed as

$$\dot{\varepsilon}^{ss} = A_0\left(\frac{\sigma_m}{G}\right)^n e^{\left(\frac{-Q}{RT}\right)}, \tag{7}$$

where $R$ is the gas constant in J/(mol·K), $T$ is the temperature in K, $\sigma_m$ is the von Mises stress in Pa, and $G$ is the shear modulus in Pa. The activation energy $Q = 270000$ J/mol, with the material constants $A_0 = 3.14\times10^{24}\ s^{-1}$ and $n = 5$.

The irradiation creep model is given as

$$\dot{\varepsilon}^{ir} = C_0\phi^{C_1}\left(\sigma_m\times10^{-6}\right)^{C_2}, \tag{8}$$

where $\dot{\varepsilon}^{ir}$ is the irradiation creep strain rate in 1/s, $\sigma_m$ is the von Mises stress in Pa, and $\phi$ is the fast neutron flux in n/($m^2$·s), with $C_0 = 9.881\times10^{-28}$, $C_1 = 0.85$, and $C_2 = 1.0$.

### The Plasticity Model Considering the Irradiation Hardening Effects

The plasticity model is expressed as (Hales et al., 2016)

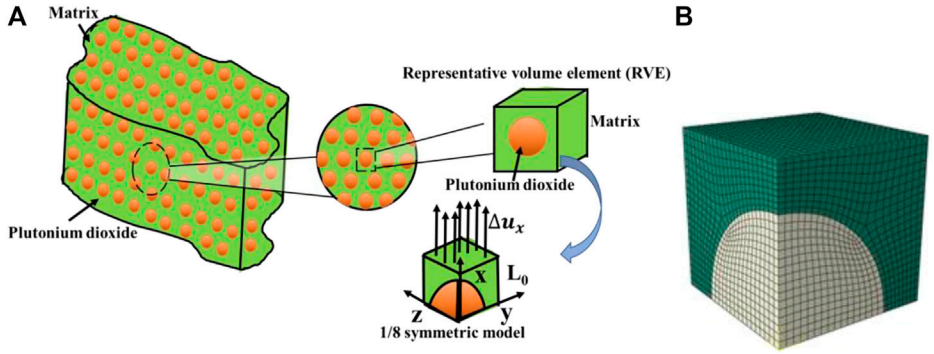


**FIGURE 1 | (A)** Development of a finite element model and **(B)** mesh grid.

$$\sigma = K\varepsilon^n \cdot \left(\frac{\dot{\varepsilon}}{10^{-3}}\right)^m, \tag{9}$$

$$K = 1.17628 \times 10^9 + T\left[4.54859 \times 10^5 + T\left(-3.28185 \times 10^3 + 1.72752T\right)\right] + K_2, \tag{10}$$

$$K_2 = 5.54 \times 10^{-18}\phi \cdot t, \tag{11}$$

$$n = \left\{-9.49 \times 10^{-2} + T\left(1.165 \times 10^{-3} + T\left(-1.992 \times 10^{-6} + 9.588 \times 10^{-10}T\right)\right)\right\} \cdot K_3, \tag{12}$$

$$K_3 = 1.369 + 0.032 \times 10^{-25}\phi \cdot t, \tag{13}$$

$$m = 0.02, \tag{14}$$

where $\sigma$ represents the true stress in Pa, and$\varepsilon$ and $\dot{\varepsilon}$ are the true strain and its rate, respectively. If $\dot{\varepsilon} < 10^{-5}$/s, set $\dot{\varepsilon} = 10^{-5}$/s. The parameters of $K$, $n$, and $m$ depict the strength coefficient, strain-hardening exponent, and strain rate sensitivity exponent, respectively. $T$ denotes the temperature in K, and $\phi \cdot t$ depicts the fast neutron fluence in n/m$^2$.

## The Finite Element Model

To establish the finite element model, it is assumed that the $PuO_2$ fuel particles are cubically distributed in a large metal matrix. Then, the representative volume element (RVE) can be selected as that in **Figure 1A**, which consists of a particle with a radius of 0.05 mm and the external matrix. According to the mean-field theory, the RVE should satisfy the periodic constraint conditions (Hill, 1963), which are satisfied by setting all surfaces of the RVE to maintain as planes. It can be known that the RVE contains all the meso-structure information of metal matrix fuels, so the effective performances can be obtained by combining the FE analysis with the homogenization method. On account of the symmetry in the RVE, 1/8 fraction of the RVE is selected as the finite element model, also shown in **Figure 1A**. The mesh grid is displayed in **Figure 1B**, with enough computational precision.

The irradiation processes are first simulated; after that, the postirradiation uniaxial tensile tests are virtually carried out, with the prescribed displacement applied along the stretch direction.

The boundary conditions for simulation of the irradiation process are described as follows. The symmetric boundary conditions are applied as follows: all the nodes on the surface of $x = 0$ satisfy $u_x = 0$, all the nodes on the surface of $y = 0$ satisfy $u_y = 0$, and all the nodes on the surface of $z = 0$ satisfy $u_z = 0$. All the nodes ($n$ nodes) on the surfaces of $x = L_0$, $y = L_0$, or $z = L_0$ have identical normal displacement components.

The fuel particle fission rate is set as $1 \times 10^{20}$ fissions/(m$^3$·s), and the fast neutron flux is set as $2.01568 \times 10^{11}$ n/(mm$^2$·s) in this study (Gong et al., 2014). It should be noticed that the fission density in fissions/m$^3$ is used to describe the experienced irradiation history in this study. With the above data of fission rate and fast neutron flux, the irradiation doses of the fuel particles and matrix can be related to the fission density.

As for the virtual postirradiation uniaxial tensile tests, the incremental displacement of $0.1L_0$ along the $x$ direction is applied on the surface of $x = L$, described as $\Delta u_x^1 = \Delta u_x^2 = \cdots = \Delta u_x^n = 0.1L_0$. It is noted that the incremental displacement of $0.1L_0$ is reached through a number of time increments. The other boundary conditions are set the same as those for the virtual irradiation process. The constant temperature is considered, which is ranged from 473 to 773 K. It should also be mentioned that the particles, the matrix, and the interface between them are assumed to be intact in this study.

## Homogenization Algorithm for Postirradiation Effective Elastoplastic Curves

According to the mean-field theory (Sanchez-Palencia and Zaoui, 1987; SemihPerdahcıoglu and Hubert, 2011), the macroscopic stresses and strains can be derived by averaging the mesoscopic ones over the volume of the finite element model as

$$\overline{\sigma}_{ij} = \frac{1}{V}\int_V \sigma_{ij} dV, \qquad \overline{\varepsilon}_{ij} = \frac{1}{V}\int_V \varepsilon_{ij} dV, \tag{15}$$

where $\overline{\sigma}_{ij}$ and $\overline{\varepsilon}_{ij}$ depict the macroscopic effective stress and strain components, respectively; $\sigma_{ij}$ and $\varepsilon_{ij}$ are the mesoscopic stress and

strain components, respectively; and $V$ is the postirradiation volume in this study.

For the considered metal-matrix composite fuel, **Eq. 15** can be expressed as

$$\begin{aligned}\overline{\sigma}_{ij} &= \overline{\sigma}^{f}_{ij} f_v + \overline{\sigma}^{m}_{ij} f_m,\\ \overline{\varepsilon}_{ij} &= \overline{\varepsilon}^{f}_{ij} f_v + \overline{\varepsilon}^{m}_{ij} f_m,\end{aligned} \tag{16}$$

where $\overline{\sigma}^{f}_{ij}$ and $\overline{\sigma}^{m}_{ij}$ are the averaged stresses of the particle and matrix over their postirradiation volumes during tensile tests, respectively; $\overline{\varepsilon}^{f}_{ij}$ and $\overline{\varepsilon}^{m}_{ij}$ denote the effective strains of the particle and matrix over their postirradiation volumes, respectively; $f_v$ indicates the current volume fraction of the particle; and $f_m$ is the current volume fraction of the matrix.

In this study, the $x$ direction is the tensile direction, so the effective stresses along the tensile direction is

$$\overline{\sigma}_x = \overline{\sigma}^{f}_{x} f_v + \overline{\sigma}^{m}_{x} f_m, \tag{17}$$

where $\overline{\sigma}^{f}_{x}$ and $\overline{\sigma}^{m}_{x}$ represent the effective stresses of the particle and matrix along the $x$ direction, respectively. It is noted that the effective stresses of the particle and matrix are obtained by the self-developed subroutines, calculated as

$$\begin{aligned}\overline{\sigma}^{f}_{x} &= \frac{\sum_{i=1}^{n_f} \sigma^{f}_{x,i} V^{f}_{i}}{V^{f}},\\ \overline{\sigma}^{m}_{x} &= \frac{\sum_{j=1}^{n_m} \sigma^{m}_{x,j} V^{m}_{j}}{V^{m}},\end{aligned} \tag{18}$$

where $n_f$ and $n_m$ are the total element numbers of the particle and matrix, respectively; $\sigma^{f}_{x,i}$ and $\sigma^{m}_{x,j}$ are the integration point stress of the $i$th particle element and $j$th matrix element along $x$ direction, respectively; $V^{f}_{i}$ and $V^{m}_{j}$ are the element volume of the particle and matrix, respectively; $V^f$ and $V^m$ are the current total volume of the particle and matrix, respectively.

The macroscopic effective strain along the stretching direction can also be calculated through the dimensional change of the finite element model during the uniaxial tensile tests, given as

$$\overline{\varepsilon}_x = \ln\left(1 + \frac{\Delta L_x}{L_0 + \Delta L^{irr}_x}\right), \tag{19}$$

where $\overline{\varepsilon}_x$ represents the macroscopic effective strain along the stretching direction; $\Delta L_x$ is the absolute length change with respect to $L_0 + \Delta L^{irr}_x$ after irradiation, which should be calculated by excluding the irradiation-induced length change, which can be expressed as

$$\Delta L_x = \Delta L^{\text{total}}_x - \Delta L^{irr}_x, \tag{20}$$

where $\Delta L^{\text{total}}_x$ is the total length change with respect to the original length of $L_0$, and $\Delta L^{irr}_x$ is the length change at the end of irradiation process, also with respect to the original length of $L_0$.

Based on the calculated effective true stresses and true strains, the postirradiation effective stress–strain curves can be obtained for various test conditions.

## Verification of the Obtained Effective Elastoplastic Property

To evaluate the computation effectiveness of the obtained macroscale elastoplastic property, the virtual loading tests for the multiparticle model and the homogenization model are implemented, using the verification method adopted by Gavrikov et al. (2018).

The effective elastoplastic constitutive relation for the case with a particle fission density of $8.64 \times 10^{26}$ fissions/m$^3$, a temperature of 573 K, and an initial particle volume fraction of 20% is obtained as

$$\overline{\sigma}_x = \begin{cases} E_{eff}\overline{\varepsilon}_x & \overline{\sigma}_x < \overline{\sigma}_{\text{yield}} \\ 733.66791\overline{\varepsilon}^{0.14369}_{x} & \overline{\sigma}_x \geq \overline{\sigma}_{\text{yield}} \end{cases}, \tag{21}$$

where $\overline{\sigma_x}$ is the effective stress along the tensile direction in MPa, $\overline{\varepsilon_x}$ is the effective strain along the tensile direction, $\overline{\sigma}_{yield}$ is the yield strength in MPa, and $E_{eff}$ represents the effective elastic modulus in MPa. In the three-dimensional simulation of the loading process for the homogenized model, it is noted that the effective stress is regarded as the Mises stress. The J2 elastoplastic constitutive theory (Azoti et al., 2013; Mantari and Canales, 2020) is adopted to correlate the three-dimensional mechanical constitutive relation with the obtained uniaxial-tension macroscale stress–strain relation. The stress update algorithm and consistent stiffness modulus could be similarly developed.

The postirradiation effective elastic modulus is given as

$$E_{eff} = 0.9071\, E^{0}_{eff}, \tag{22}$$

where $E^{0}_{eff}$ denotes the effective elastic modulus before irradiation, calculated with the Mori–Tanaka model (Budiansky and Wu, 1961):

$$E^{0}_{eff} = \frac{9K_{eff}G_{eff}}{3K_{eff} + G_{eff}}, \tag{23}$$

where $K_{eff}$ and $G_{eff}$ are effective bulk modulus and shear modulus, respectively, expressed as

$$\begin{aligned}K_{eff} &= K_m\left[1 + \frac{f_{v0}\left(K_f/K_m - 1\right)}{1 + \alpha\left(1 - f_{v0}\right)\left(f_{v0}/K_m - 1\right)}\right]\\ G_{eff} &= G_m\left[1 + \frac{f_{v0}\left(G_f/G_m - 1\right)}{1 + \beta\left(1 - f_{v0}\right)\left(G_f/G_m - 1\right)}\right],\end{aligned} \tag{24}$$

where $K$ and $G$ depict the bulk modulus and shear modulus, with subscripts of $f$ and $m$ representing the particle and matrix, respectively; $f_{v0}$ is the initial particle volume fraction; and $\alpha$ and $\beta$ are denoted as

$$\begin{aligned}\alpha &= \frac{1}{3}\frac{1+\mu_m}{1-\mu_m},\\ \beta &= \frac{2}{15}\frac{4-5\mu_m}{1-\mu_m},\end{aligned} \tag{25}$$

where $\mu_m$ is Poisson's ratio of matrix.

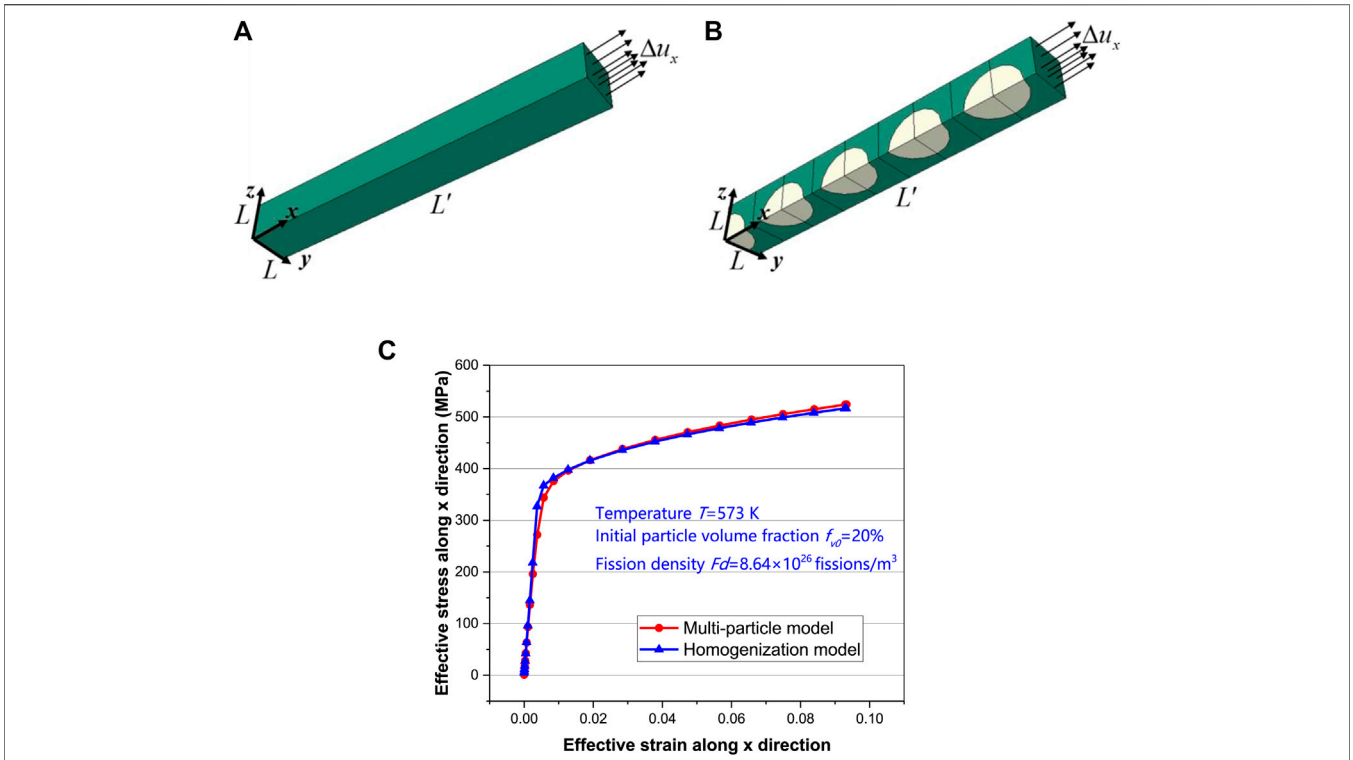


**FIGURE 2 | (A)** Homogenization model, **(B)** a multiparticle model, and **(C)** verification of the effective elastoplastic constitutive relations.

To verify the effectiveness of **Eq. 21**, the homogenization model is established, as shown in **Figure 2A**. The simulations of irradiation tests and postirradiation loading are performed. The deformations of elastic, plastic, and irradiation swelling are taken into account for the mechanical constitutive relation of the irradiation simulation test. In simulation of the postirradiation loading, the postirradiation elastoplastic constitutive model is adopted. It should be mentioned that the effective swelling model has been used in simulation of the irradiation process, which has been developed and verified in our recent study (Zhang et al., 2021). Thus, the results can be compared with those calculated through the multiparticle model displayed in **Figure 2B**, which is 1/8 of the model with nine particles.

### Simulation of the Irradiation Process and Postirradiation Uniaxial Tension

The mechanical boundary conditions are similar as those in *the Finite Element Model*. In the irradiation process, all the nodes on the surface of $x = 0$ satisfy $u_x = 0$, all the nodes on the surface of $y = 0$ satisfy $u_y = 0$, and all the nodes on the surface of $z = 0$ satisfy $u_z = 0$. All the nodes ($n$ nodes) on the surfaces of $x = L^{'}$, $y = L$, or $z = L$ have identical normal displacement components. As for the postirradiation uniaxial tensile test, the incremental displacement of $\Delta u_x = 0.1L^{'}$ along the $x$ direction is applied on the surface of $x = L^{'}$, where $L^{'}$ is the initial length of the model. The other boundary conditions are also set the same as those for the virtual irradiation process.

The particle size is the same as previously mentioned, and the homogenization model is in the same size as that of the multiparticle model. The comparison results are shown in **Figure 2C**. It can be seen that the results agree well with each other. The maximum relative error occurs at the initial yield stage, which is ~6.85%, and is within the acceptable range. The results indicate that the effective elastoplastic properties are valid, and the multi-scale simulation method is feasible.

### Simulation of the Irradiation Process and Postirradiation Multiaxial Loading

In order to better simulate the mechanical state of fuel in the reactor, a pressure of 20 MPa is applied to the outer surfaces of the homogenization model and the multiparticle model, which is described as on the surface of $z = L$: pressure $p = 20$ MPa, and on the surface of $y = L$: pressure $p = 20$ MPa. The pressure is set to maintain constant in the whole tensile process.

The effective strains along the $x$ direction and the $y$ direction of these two models are given in **Figure 3**, and the coordinate of horizontal axis depicts the ratio of displacement along the $x$ direction to the initial length $L^{'}$. It can be known that the deformations along the $x$ direction and the $y$ direction of the multiparticle model are the same as those of the homogenization model, which also implies the availability of the effective elastoplastic properties.

## INFLUENCE FACTORS OF POSTIRRADIATION EFFECTIVE STRESS–STRAIN CURVES

The $x$-direction effective stress–strain curve for a case can be found in **Figure 4**, which gives the results of the tensile test after

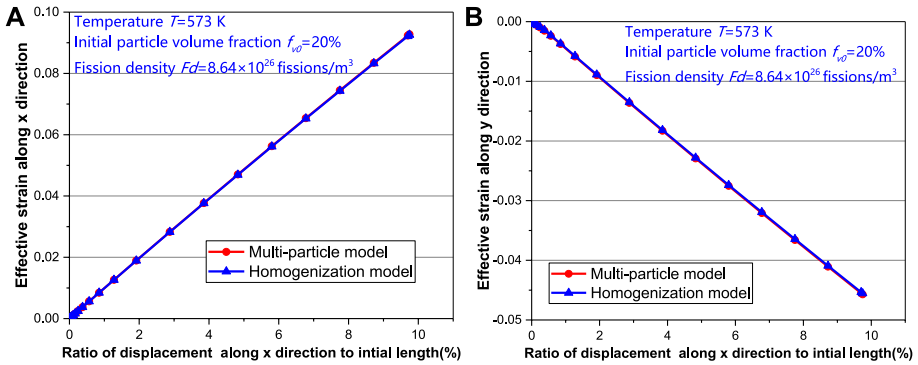


**FIGURE 3 |** Effective strains along **(A)** the *x* direction and **(B)** *y* direction.

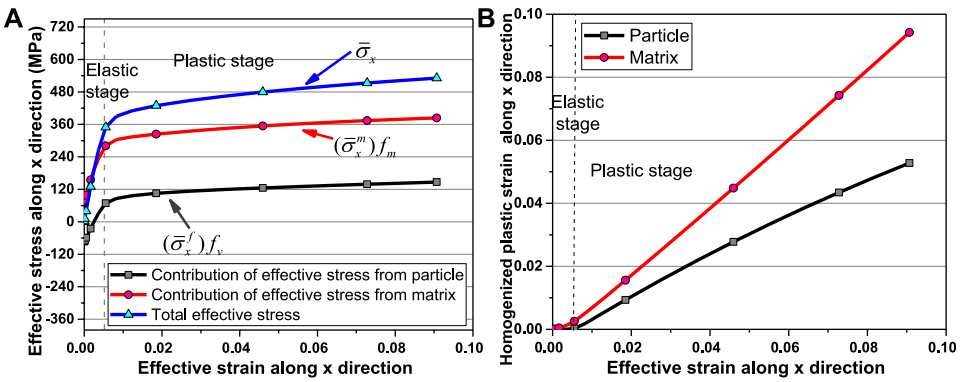


**FIGURE 4 | (A)** Effective stress/strain curves and the effective stress contributions and **(B)** the homogenized plastic strains along the *x* direction during the tensile test.

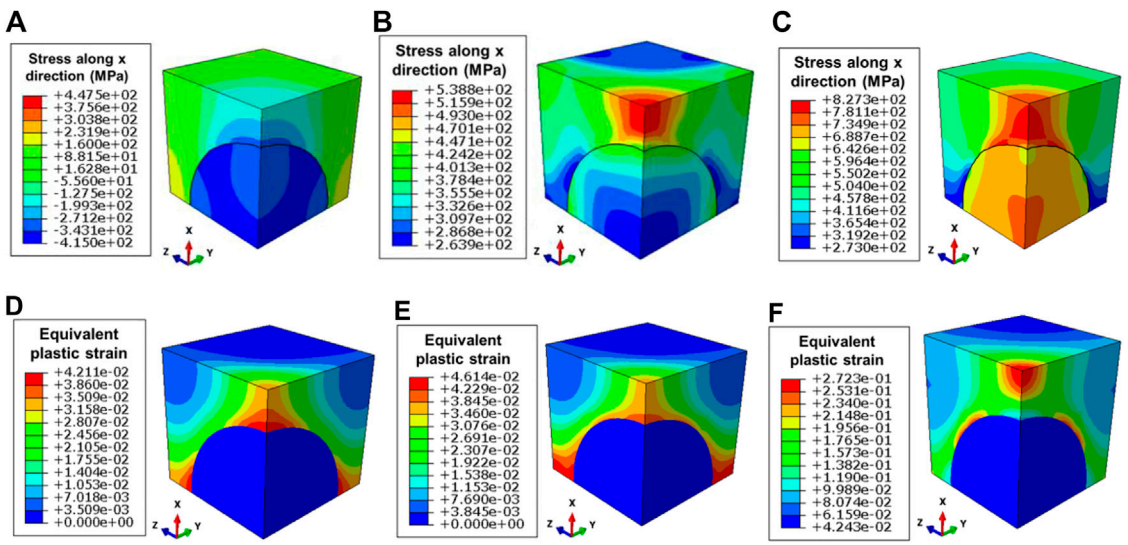


**FIGURE 5 |** Stresses along the *x* direction at the end of the **(A)** irradiation, **(B)** quasi-elastic stage, and **(C)** the whole tensile stage, the equivalent plastic strains at the end of the **(D)** irradiation, **(E)** quasi-elastic stage, and **(F)** whole tensile stage.

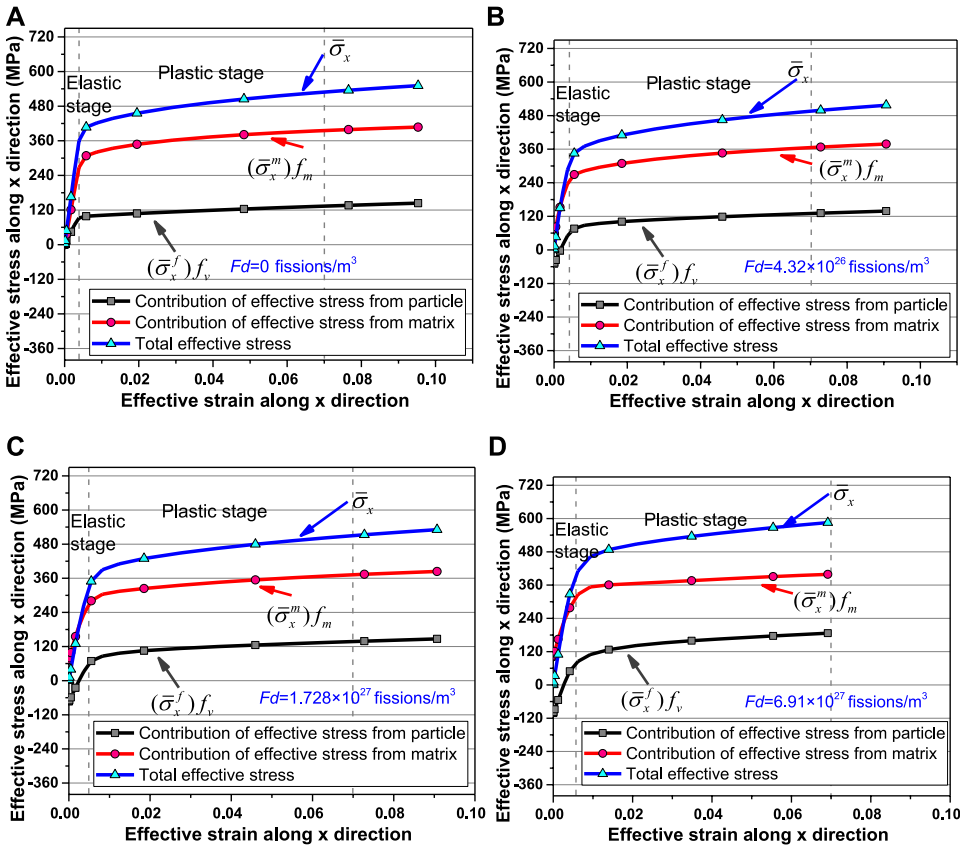


**FIGURE 6 |** Effective stress/strain curves and the effective stress contributions for the particle fission density of **(A)** 0 fissions/m$^3$, **(B)** 4.32 × 10$^{26}$ fissions/m$^3$, **(C)** 1.728 × 10$^{27}$ fissions/m$^3$, and **(D)** 6.91 × 10$^{27}$ fissions/m$^3$.

irradiation of 1.728 × 10$^{27}$ fissions/m$^3$. This stress/strain curve can be divided into two stages of quasi-elastic one and plastic one. The stress and strain obey an approximately linear relation in the quasi-elastic stage, with a high increase of stress and a relatively small effective strain increment. After that, the deformation resistance of composite fuel is weakened.

From **Figure 4A**, one can also see the effective stress contributions from matrix and particle, denoted as $(\overline{\sigma}_x^m)f_m$ and $(\overline{\sigma}_x^f)f_v$. The explanations for the variables of $\overline{\sigma}_x^m$, $\overline{\sigma}_x^f$, $f_m$, and $f_v$ can be found in *the Finite Element Model*. For the reason that the current particle volume fraction of 21% is much lower than the matrix occupancy, the effective stresses are largely contributed by the matrix. In the quasi-elastic stage, the homogenized *x*-direction plastic strains of the particle and matrix are negligible, as given in **Figure 4B**. In the plastic stage, the *x*-direction effective plastic strains of the particle and matrix are continuously enlarged, while the increment rate of effective stress is much smaller than that in the elastic stage.

This appearance of the postirradiation mechanical response is closely related to the residual stress/strain states just after irradiation. The contour plots of *x*-direction stress and equivalent plastic strain are displayed in **Figure 5**, respectively. In **Figures 5A–C**, the *x*-direction stresses just after irradiation are presented, together with those at the end of the quasi-elastic stage and the tensile test. One can see that the particle is compressed just after irradiation, with high compressive stresses. Although a major part of the matrix is

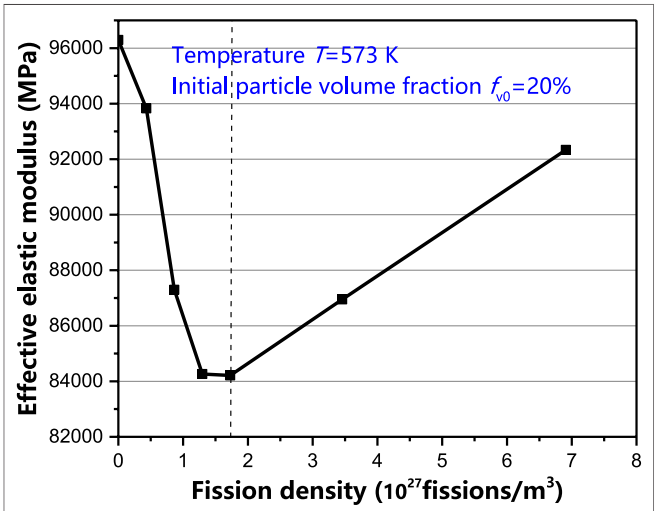


**FIGURE 7 |** Postirradiation effective elastic modulus as a function of particle fission density.

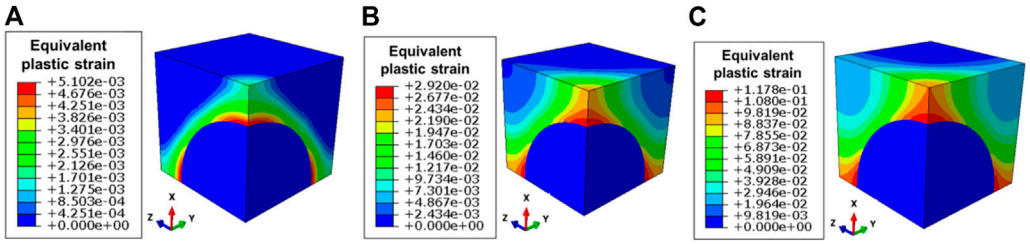


**FIGURE 8 |** Equivalent plastic strains just after irradiation of **(A)** 4.32 × $10^{26}$ fissions/$m^3$, **(B)** 1.296 × $10^{27}$ fissions/$m^3$, and **(C)** 3.456 × $10^{27}$ fissions/$m^3$.

in tension, the local region above the particle is also subjected to *x*-direction compressive stresses. During postirradiation tension, the stresses are redistributed. At the end of the quasi-elastic stage, the stresses in the particle turn into larger tensile stresses. The stress distribution in the matrix also changes greatly, with the originally compressive region turned into the maximum tensile stress one. When the whole tensile test ends, the tensile stresses in the particle have an obvious increase. The tensile stress region in the matrix further expands, and the peak value increases distinctly.

The existence of the long quasi-elastic stage can be explained by the results in **Figures 5D–F**. **Figure 5D** depicts that the plastic deformation has only occurred in the matrix after irradiation, and large equivalent plastic strains appear in the matrix region surrounding the particle. At the end of the quasi-elastic stage, no plastic strains are produced in the particle although the maximum increment of *x*-direction stress exceeds ~800 MPa. The equivalent plastic strains in the matrix have slight increments. The original regions of compressive stress make the composite to have a relatively large value of *x*-direction

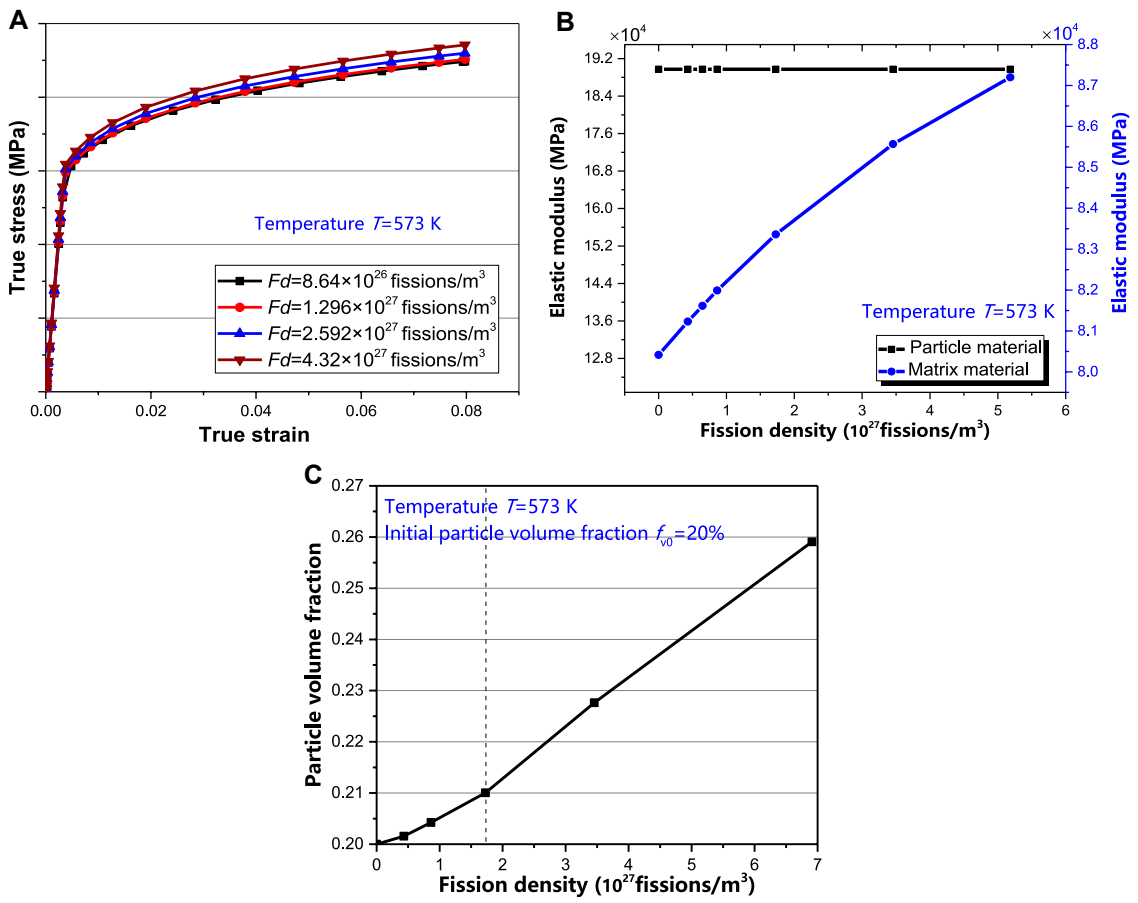


**FIGURE 9 | (A)** True stress–strain curves of the metal matrix material, **(B)** the elastic modulus of the particle material and matrix material, and **(C)** the particle volume fraction after different fission densities.

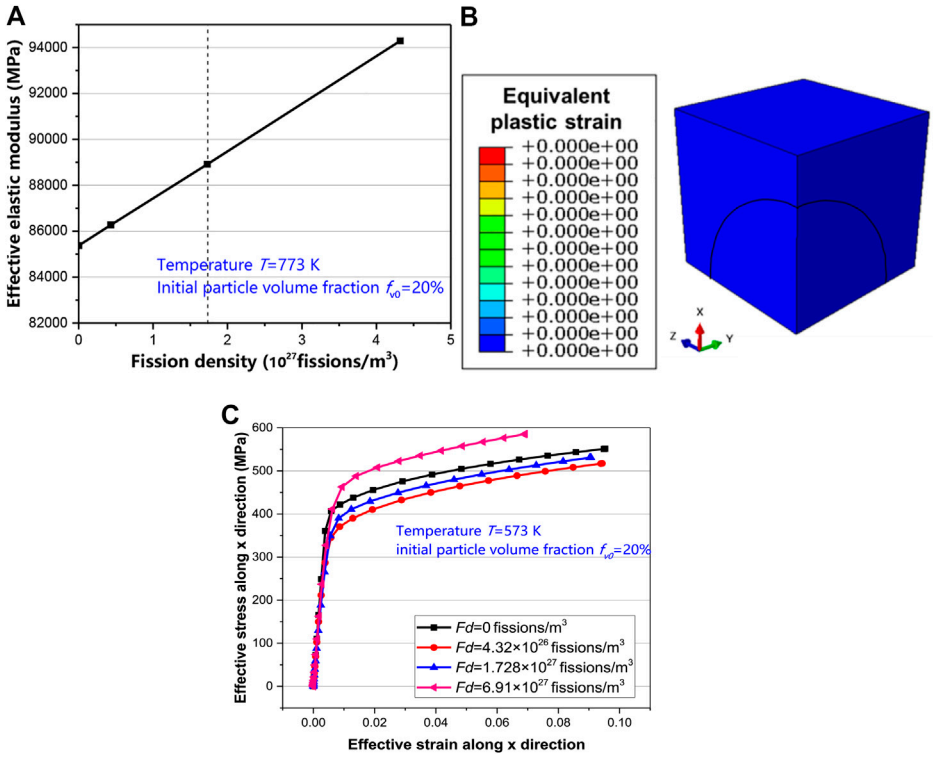


**FIGURE 10 |** Postirradiation **(A)** effective elastic modulus and **(B)** equivalent plastic strain of the composite after irradiation of 4.32 × $10^{26}$ fissions/$m^3$ and **(C)** effective elastoplastic curves after different fission densities.

effective strain in the quasi-elastic stage, without producing large new plastic deformations. However, it should be noted that new equivalent plastic strains occur in the original irradiation-induced tensile stress region, which means that some points have undergone the plastic loading process in the quasi-elastic stage. From **Figure 5F**, one can observe that new plastic strains take place in both the particle and matrix. Especially, the maximum equivalent plastic strain in the matrix becomes ~6.47 times of that just after irradiation, and the occupied region has shifted from the one adjacent to the particle to the new red-colored one.

Based on the obtained postirradiation elastoplastic curves, the effective elastic modulus, the effective yield strength, and effective hardening functions can be determined. In this section, the effects of particle fission density, temperature, and initial particle volume fraction are given, and the influence mechanisms are analyzed.

## Effects of Particle Fission Density

To analyze the irradiation dose on the postirradiation mechanical response, the effective stress–strain curves for various particle fission densities are displayed in **Figure 6**, together with the effective stress contributions from the particle and matrix. It is noted that these curves represent the results for the case with a test temperature of 573 K and an initial particle volume fraction of 20%. In the four investigated cases, the unirradiated composite has the maximum curve slope of the quasi-elastic stage. With the increase of particle fission density, the slopes of this stage tend to decrease first and then rise, which results from the change of matrix curve slopes. Additionally, the elastic stage is enlarged for the fission density of 6.91 × $10^{27}$ fissions/$m^3$.

The effective stress contributions from particle and matrix are also presented in **Figure 6**. It can be seen that the effective stress contribution from matrix is greater than that from particle. For the curve point with an effective true strain of 0.07, the effective stress from the matrix accounts for 74.87% of the total effective stress of the unirradiated composite, while the ratio is 68.12% for the fission density of 6.91 × $10^{27}$ fissions/$m^3$. The yield strength of the composite fuel also changes with fission density, mainly affected by the postirradiation mechanical performances of the matrix. Besides, the decrease of the matrix volume fraction owing to irradiation swelling of the particle plays a certain role, as analyzed in the following.

The effective stresses in the quasi-elastic stage are almost linearly related to the effective strains, which are described in terms of elastic modulus. **Figure 7** shows the effective elastic modulus as a function of particle fission density. One can find that the effective elastic modulus decreases first, and after 1.728 × $10^{27}$ fissions/$m^3$, it gradually increases. When the particle fission density exceeds the considered maximum value, the postirradiation effective elastic modulus might be larger than that of the unirradiated case. The effective elastic

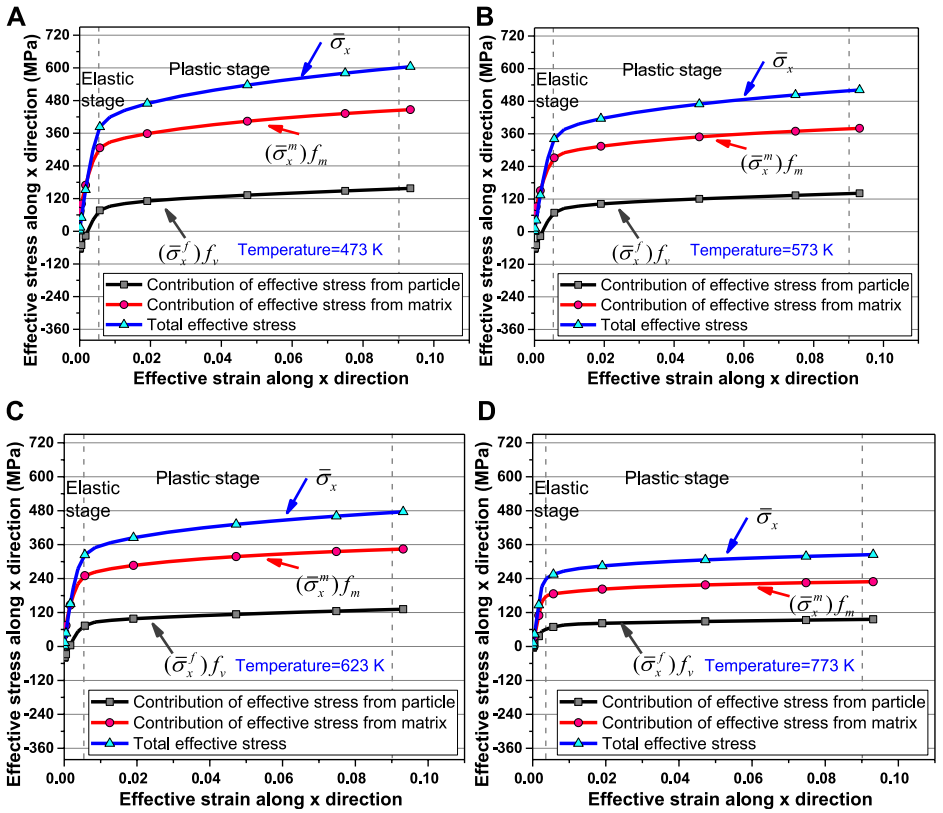


**FIGURE 11 |** Effective stress/strain curves and the effective stress contributions under the test temperature of **(A)** 473 K, **(B)** 573 K, **(C)** 623 K, and **(D)** 773 K.

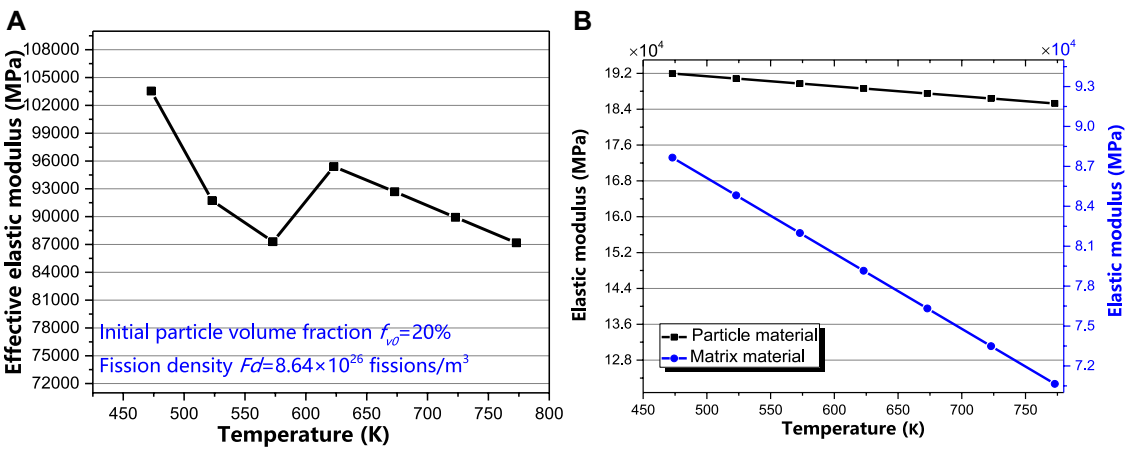


**FIGURE 12 | (A)** Postirradiation effective elastic modulus under different temperatures and **(B)** the elastic modulus of the particle material and matrix material.

modulus is defined as the ratio of effective stress to effective strain, namely,

$$E_{eff} = \frac{\bar{\sigma}_x}{\bar{\varepsilon}_x}, \tag{26}$$

where $\bar{\sigma}_x$ and $\bar{\varepsilon}_x$ are effective stress and effective strain along the tensile direction, respectively. It should also be mentioned that the effective strain selected to calculate the effective modulus is less than $5 \times 10^{-4}$ in order to guarantee the deformation is in the quasi-elastic stage.

The equivalent plastic strain plots of the particle and matrix for three cases are displayed in **Figure 8**, which are the results obtained just before performing the subsequent tension. It can be seen that the equivalent plastic strains in the matrix increase

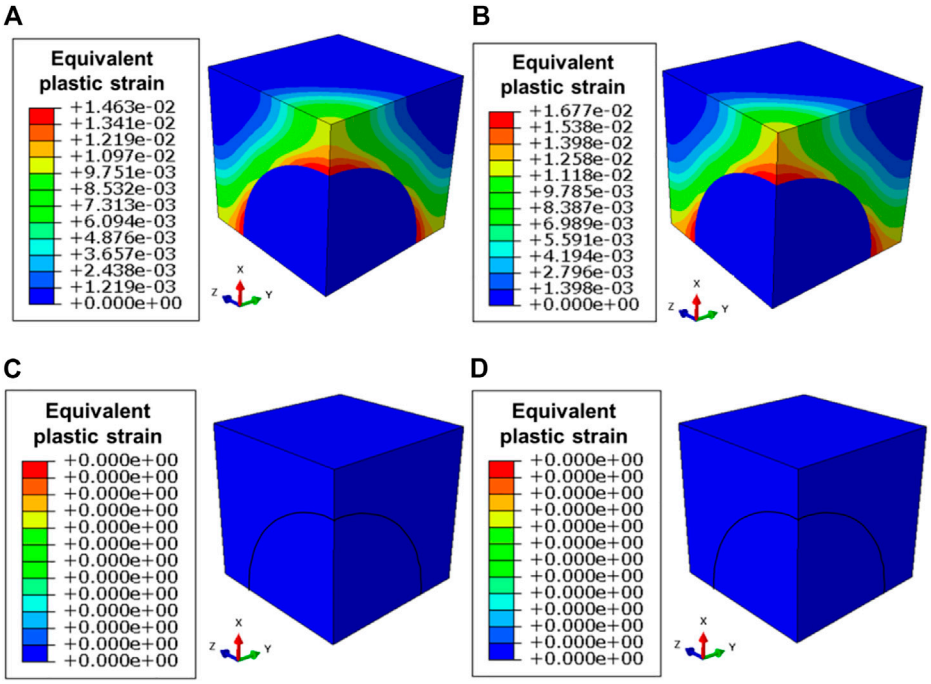


**FIGURE 13 |** Equivalent plastic strains after irradiation of 8.64 × $10^{26}$ fissions/$m^3$ at temperatures of **(A)** 473 K, **(B)** 573 K, **(C)** 623 K, and **(D)** 773 K.

obviously with the particle fission density. During the postirradiation uniaxial tension, the incremental stress/strain constitutive relations will vary with the achieved equivalent plastic strains for all the points. If the points undergo further plastic loading, the elastoplastic constitutive relation will be obeyed. When the unloading process occurs, the increments of stresses and strains satisfy the elastic constitutive relation. The stress–strain curves of the metal matrix material are displayed in **Figure 9A**, with the irradiation hardening effects considered. The slopes of the curves decrease with the equivalent plastic strain and give rise to the particle fission density. So, a competition exists between the effects of plastic strain softening and irradiation hardening. As shown in **Figure 6**, the quasi-elastic stage slope of effective stress–strain curves for the matrix decreases with the particle fission density before 1.728 × $10^{27}$ fissions/$m^3$, because the plastic strain softening effects dominate. As mentioned previously, some points in the matrix experience plastic loading in the quasi-elastic stage, which results in a decrease in the quasi-elastic stage slope. From 1.728 × $10^{27}$ fissions/$m^3$ to 6.91 × $10^{27}$ fissions/$m^3$, the quasi-elastic stage slope for the matrix is enlarged. On the one hand, the elastic modulus of the matrix and the slope of the hardening curve both grow with irradiation dose. On the other hand, the current particle volume fraction also increases with the particle fission density.

With the increase of particle fission density, the elastic modulus of the matrix gradually increases, as shown in **Figure 9B**. The elastic modulus of the matrix at the fission density of zero and 5.184 × $10^{27}$ fissions/$m^3$ is about 80.42 and 87.2 GPa, respectively. As depicted in **Figure 9B**, the elastic modulus of the particle material is ~189.73 GPa, which is much greater than that of the matrix material. When the fission density is 5.184 × $10^{27}$ fissions/$m^3$, the elastic modulus of the particle is 2.18 times as much as that of the matrix. As the particle fission density is increased, due to the accumulated irradiation swelling of the particle, its current volume fraction gradually increases. In **Figure 9C**, one can see that the increasing rate of particle volume fraction is small at lower fission densities, and then larger increasing rate maintains. At the particle fission density of 6.91 × $10^{27}$ fissions/$m^3$, the particle volume fraction increases by 29.54%. After the particle fission density of 1.728 × $10^{27}$ fissions/$m^3$, the enlarged fuel particle provides higher deformation resistance. As a result, the variation phenomenon of effective elastic modulus in **Figure 7** can be explained.

The postirradiation effective elastic modulus as a function of fission density can be found in **Figure 10A**, which is obtained for the test temperature of 773 K. It can be seen that the effective elastic modulus increases monotonically with particle fission density, different from the dependence relation shown in **Figure 7**. As shown in **Figure 10B**, no plastic deformation occurs in the matrix after irradiation of 4.32 × $10^{26}$ fissions/$m^3$, owing to the stress relaxation effect of creep. Therefore, in the elastic stage of postirradiation tension, the plastic strain softening effect of the matrix on the effective elastic modulus disappears. Meanwhile, it can be concluded that the postirradiation mechanical response of composite fuels will vary with the irradiation temperature.

**Figure 10C** depicts the effective elastoplastic curves for various cases of particle fission density. One can see that the

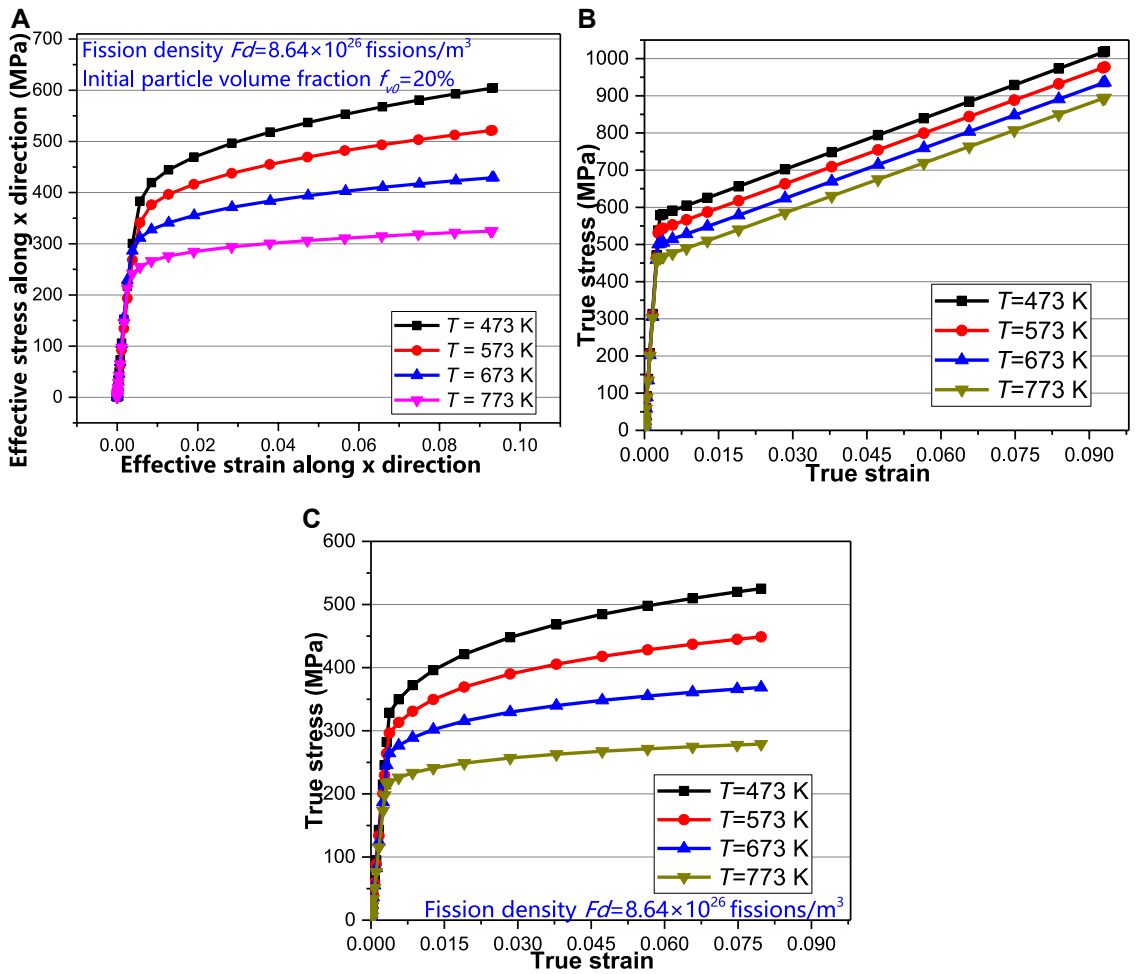


**FIGURE 14 |** Postirradiation **(A)** effective elastoplastic curves, **(B)** stress–strain curves of $PuO_2$, and **(C)** stress–strain curves of the matrix material under different temperatures.

effective yield strengths present the same variation phenomenon with the particle fission density, as that in **Figure 7**. The plastic strain softening and irradiation hardening effects compete in the $PuO_2$/Zr composite fuel for the test temperature of 573 K, which results from the accumulated equivalent plastic strains in the matrix, the irradiation hardening effects of the matrix, and the increase of particle volume fraction. It should be mentioned that the plastic strain softening effects at higher irradiation temperatures will not occur.

## Effects of Temperature

The effective stress–strain curves for different temperatures are shown in **Figure 11**, together with the effective stress contributions from the particle and matrix. These results are for the cases with a particle fission density of $8.64 \times 10^{26}$ fissions/$m^3$ and an initial particle volume fraction of 20%. As a whole, the curve slopes of the quasi-elastic stage decrease with temperature. When the temperature is increased from 623 to 773 K, the elastic stage decreases significantly, and the slope of the effective stress–strain curve is also greatly reduced. The yield strengths are lessened and the strain hardening effects are weakened at higher temperatures.

The effective stress contributions from the particle and matrix are also displayed in **Figure 11**. Effective stress of matrix has a larger contribution than that of the particle, owing to its higher volume fraction of ~80%. For the effective strain of 0.09, the effective stress of the matrix to the total effective stress, that is, $\overline{\sigma}_x^m f_m/\overline{\sigma}_x$, is 73.9% at 473 K, while the relative ratio is 70.49% at 773 K. The effective stresses at a higher temperature are obviously reduced, which dominantly result from the weakened deformation resistance of the metal matrix. It is noted that the current particle volume fraction has slight differences for the considered cases in this section, so the analysis will not focus on it.

In order to analyze the behavior of the quasi-elastic stage, the effective elastic moduli are obtained for different temperature cases. As depicted in **Figure 12A**, the effective elastic modulus first decreases with temperature, increases from 573 to 623 K, and then decreases almost linearly with temperature from 623 to 773 K. The effective elastic modulus at 773 K is ~87 GPa. This

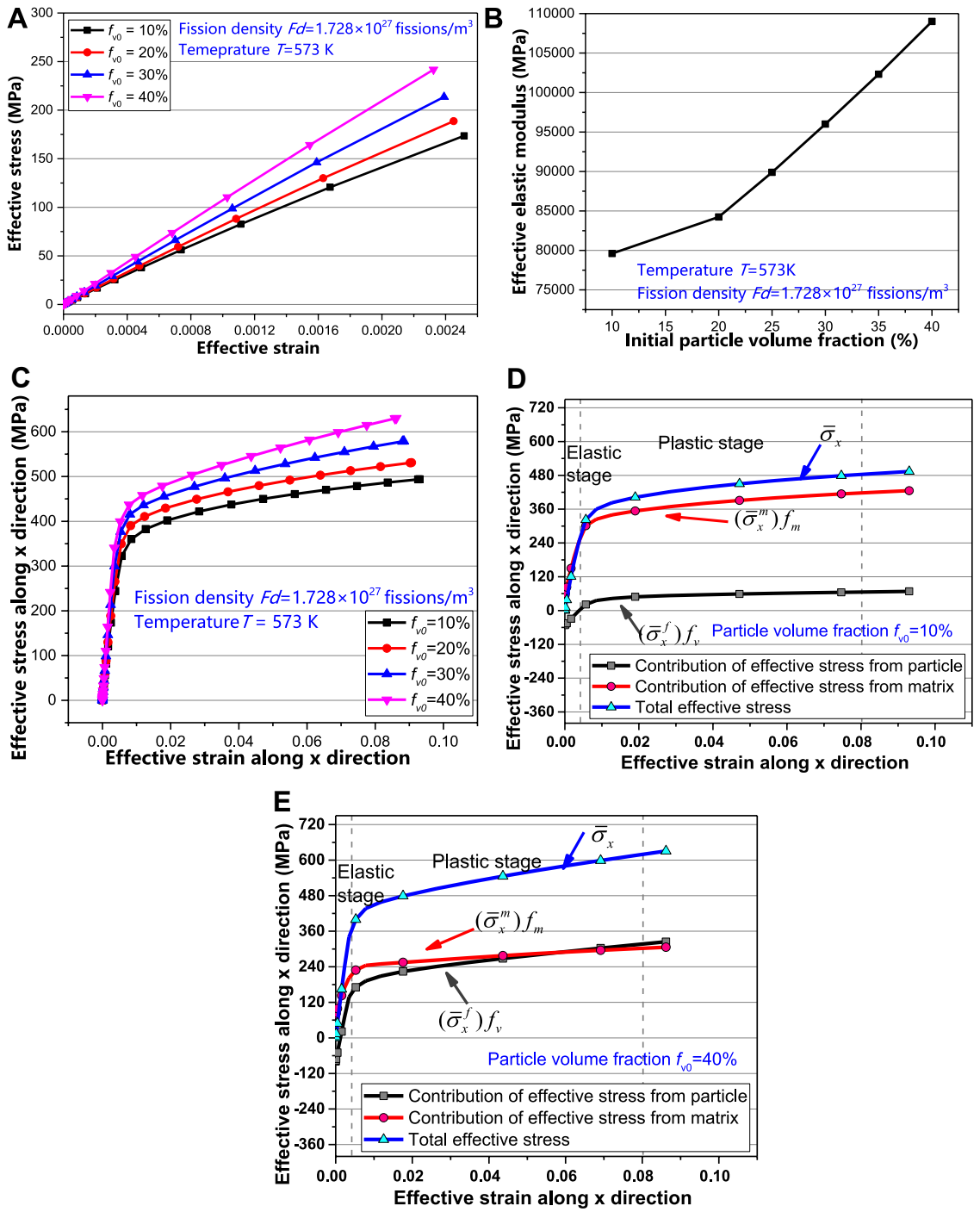


**FIGURE 15 |** Postirradiation **(A)** effective stress–strain curves of the elastic stage, **(B)** elastic modulus, and **(C)** effective elastoplastic curves under different initial particle volume fractions, the effective stress–strain curves, and the contribution from the particle and matrix for the initial particle volume fractions of **(D)** 10% and **(E)** 40%, respectively.

variation law depends on the irradiation-induced equivalent plastic strains in the metal matrix.

The equivalent plastic strain plots of the particle and matrix for four temperatures are shown in **Figure 13**, which are the results just after irradiation. One can find that the regions with larger equivalent plastic strains expand with temperature from 473 to 573 K, and the maximum strains also increase with temperature. As mentioned previously, the irradiation-induced plastic deformation in the matrix will reduce the effective elastic modulus of the composite. However, when the temperature reaches 623 K or higher values, no after-irradiation plastic deformations occur in the matrix, owing to the significant

stress relaxation effects of creep deformation, which also indicates that the effective elastic modulus of composite under these temperature conditions is mainly influenced by the elastic properties of the particle and matrix.

As depicted in **Figure 12B**, the elastic moduli of both the particle material and matrix material decrease with temperature. One can find that the elastic modulus of matrix material has a great decrease rate with temperature. From 473 to 773 K, the elastic modulus of the metal matrix material decreases from 87.66 to 70.65 GPa, that is, decreased by 19.4%. However, the elastic modulus of the particle material decreases from 191.95 to 185.29 GPa, that is, decreased by 3.47%. As a result, the effective elastic modulus of the composite decreases with temperature as a whole. When the temperature increases from 573 to 623 K, the effective elastic modulus is found to have an increase, as shown in **Figure 12A**. This is due to the fact that irradiation-induced plastic strains in the matrix have a degradation effect on the effective elastic modulus of the composite at lower temperatures, while at 623 K, this effect vanishes.

The postirradiation effective elastoplastic curves under different temperatures can be found in **Figure 14A**. It can be observed directly that the effective yield strengths reduce monotonically with temperature. The effective stress at the end of the curve is 604.5 MPa at 473 K, while the stress value is 324.8 MPa at 773 K, with a decrease of 46.27%. The macroscale mechanical response is dependent on the mechanical constitutive relations of the involved materials. **Figure 14B** gives the stress–strain curves of $PuO_2$ material under different temperatures. Compared to the plastic-stage curves of the matrix in **Figure 14C**, it can be known that the temperature has a weaker effect on the hardening curves of the particle. So, the effective stress contributions from the particle are enhanced with the increase of temperature, when the corresponding contributions from the matrix are markedly reduced, as presented in **Figure 11**.

## Effects of Initial Particle Volume Fraction

**Figure 15A** gives the postirradiation effective stress–strain curves of the quasi-elastic stage for different cases of initial particle volume fractions, where $f_{v0}$ represents the initial particle volume fraction. These results in this section are for the case with a particle fission density of $1.728 \times 10^{27}$ fissions/m$^3$ and a temperature of 573 K. The ratios of effective stress to effective strain increase with the initial particle volume fraction, as depicted in **Figure 15B**. With the increase of initial particle volume fraction from 10 to 40%, the effective elastic modulus of composite fuels is increased from 79.61 to 109 GPa, with an increase of 36.92%. The increase of the effective elastic modulus is mainly induced by the enlarged particle volume fractions, because the elastic modulus of the particle material is 190.84 GPa at the temperature of 573 K, which is much larger than that of the matrix material (86.24 GPa).

The postirradiation effective elastoplastic curves for various cases of initial particle volume fraction are given in **Figure 15C**. When the initial particle volume fraction increases, the effective stresses in the plastic stage are elevated. To capture the influence mechanism of initial particle volume fraction, the effective stress contributions from the particle and matrix should be analyzed. As shown in **Figures 15D,E**, with a rise of initial particle volume fraction from 10 to 40%, the effective stress contribution of the particle has been greatly improved. When the initial particle volume fraction is 10%, the ratio of the effective stress of matrix to the total effective stress, that is, $\overline{\sigma}_x^m f_m/\overline{\sigma}_x$, is 86.2% at the end of the curve. When the initial particle volume fraction is 40%, the effective stress contribution of the matrix is a bit higher than that of the particle at first, and then the effective stress contribution of the particle exceeds that of the matrix. The ratio of the effective stress of the matrix to the total effective stress is 48.53% at the end of the curve, similar to the stress contribution of the particle. Since the deformation resistance of the particle is high, the effective stresses at the plastic stage are increased distinctly for the initial particle volume fraction of 40%.

# CONCLUSION

In this study, the postirradiation effective elastoplastic responses of metal-matrix fuels are obtained through multi-scale numerical simulation studies based on homogenization theory. The effects of particle fission density, temperature, and initial particle volume fraction are investigated. The effective stress contributions from the particle and matrix are analyzed. The conclusions can be drawn as follows.

1) At 573 K, the postirradiation effective elastic modulus and effective yield strength decrease first and then increase with the achieved particle fission density, which is related to the accumulated equivalent plastic strains in the matrix, the irradiation hardening of the matrix, and the enlarged current particle volume fraction. With the increase of temperature and initial particle volume fraction, the effective stress contribution of the particle is improved, and that of the matrix is weakened.
2) The effective elastic modulus varies non-monotonically with temperature, which results from the combined effects of after-irradiation equivalent plastic strains in the matrix, and the degradation of the elastic moduli of the particle and matrix with temperature.
3) The effective yield strength of the considered composite fuel increases with the initial particle volume fraction, due to the high plastic deformation resistance of the particle material, especially at higher temperatures.

# DATA AVAILABILITY STATEMENT

The raw data supporting the conclusion of this article will be made available by the authors, without undue reservation.

# AUTHOR CONTRIBUTIONS

JZ: software, validation, formal analysis, investigation, data curation, writing—original draft, and visualization; SD: conceptualization, methodology, software, resources, writing—review and editing, supervision, and project administration.

## FUNDING

The authors are very grateful for the supports of the National Natural Science Foundation of China (nos. 11772095 and 11572091), the support of the National Key Research and Development Program of China (2016YFB0700103), and the supports of the foundation from Science and Technology on Reactor System Design Technology Laboratory.

## REFERENCES

Abedini, A., and Chen, Z. T. (2014). A Micromechanical Model of Particle-Reinforced Metal Matrix Composites Considering Particle Size and Damage. *Comput. Mater. Sci.* 85, 200–205. doi:10.1016/j.commatsci.2014.01.012

Adamson, R. B., and Coleman, C. E. (2019). MalcolmGriffiths. Irradiation Creep and Growth of Zirconium Alloys: A Critical Review. *J. Nucl. Mater.* 521, 167–244. doi:10.1016/j.jnucmat.2019.04.021

Aoki, T., Sagara, H., and Han, C. Y. (2019). Material Attractiveness Evaluation of Inert Matrix Fuel for Nuclear Security and Non-proliferation. *Ann. Nucl. Energ.* 126, 427–433. doi:10.1016/j.anucene.2018.10.063

Azoti, W. L., Tchalla, A., Koutsawa, Y., Makradi, A., Rauchs, G., Belouettar, S., et al. (2013). Mean-field Constitutive Modeling of Elasto-Plastic Composites Using Two (2) Incremental Formulations. *Compos. Structures* 105, 256–262. doi:10.1016/j.compstruct.2013.05.044

Bouhamed, A., Jrad, H., Mars, J., Wali, M., Gamaoun, F., and Dammak, F. (2019). Homogenization of Elasto-Plastic Functionally Graded Material Based on Representative Volume Element: Application to Incremental Forming Process. *Int. J. Mech. Sci.* 160, 412–420. doi:10.1016/j.ijmecsci.2019.07.005

Budiansky, B., and Wu, T. T. (1961). Theoretical Prediction of Plastic Strains of Polycrystals. *Proc. 4th V.S. Nat. Congr. Appl. Mech.*, 1175–1185.

Byun, T. T., and Farrell, K. (2004). Irradiation Behavior of Polycrystalline Metals after Low Temperature Irradiation. *J. Nucl. Mater.* 326, 86–96. doi:10.1016/j.jnucmat.2003.12.012

Carmack, W. J., Todosow, M., Meyer, M. K., and Pasamehmetoglu, K. O. (2006). Inert Matrix Fuel Neutronic, thermal-hydraulic, and Transient Behavior in a Light Water Reactor. *J. Nucl. Mater.* 352, 276–284. doi:10.1016/j.jnucmat.2006.02.098

Chan, K. C., and Lee, W. B. (1993). Effect of Prestrain on the Evolution of Yield Locus of Polycrystalline Metals. *Adv. Eng. Plasticity its Appl.*, 547–553. doi:10.1016/b978-0-444-89991-0.50075-5

Cui, Y., Ding, S. R., Chen, Z. T., and Huo, Y. Z. (2015). Modifications and Applications of the Mechanistic Gaseous Swelling Model for UMo Fuel[J]. *J. Nucl. Mater.* 457, 157–164. doi:10.1016/j.jnucmat.2014.11.065

Ding, S., Wang, Q., and Huo, Y. Z. (2010). Mechanical Behaviors of the Dispersion Nuclear Fuel Plates Induced by Fuel Particle Swelling and thermal Effect II: Effects of Variations of the Fuel Particle Diameters[J]. *J. Nucl. Mater.* 397, 80–91. doi:10.1016/j.jnucmat.2009.12.012

Doghri, I., and Friebel, C. (2005). Effective Elasto-Plastic Properties of Inclusion-Reinforced Composites. Study of Shape, Orientation and Cyclic Response. *Mech. Mater.* 37, 45–68. doi:10.1016/j.mechmat.2003.12.007

Doghri, I., Brassart, L., Adam, L., and Gérard, J. S. (2011). A Second-Moment Incremental Formulation for the Mean-Field Homogenization of Elasto-Plastic Composites. *Int. J. Plast.* 27, 352–371. doi:10.1016/j.ijplas.2010.06.004

Duyn, L. V. (2003). *Evaluation of the Mechanical Behavior of a Metal Matrix Dispersion Fuel for Plutonium Burning*. Atlanta: Georgia Institute of Technology: A thesis for the Degree Master of Science in Mechanical Engineering.

Eshelby, J. D. (1957). The Determination of the Elastic Field of an Ellipsoidal Inclusion and Related Problems. *Proc. Roy. Soca* 241, 376–396. doi:10.1098/rspa.1957.0133

Gavrikov, A. A., Knyazkov, D., and Melnikov, A. M. (2018). On Limits of Applicability of the Homogenization Method to Modeling of Layered Creep media. *IFAC-Papers OnLine* 51 (2), 144–149. doi:10.1016/j.ifacol.2018.03.025

George, W. (2012). *Microscopic Mechanisms of Damage Caused by Degradants*. Toronto: Atlas of Material Damage, 105–283.

Gong, X., Zhao, Y. M., and Ding, S. R. (2014). A New Method to Simulate the Micro-thermo-mechanical Behaviors Evolution in Dispersion Nuclear Fuel Elements. *Mech. Mater.* 77, 14–27. doi:10.1016/j.mechmat.2014.06.004

Hales, J. D., Williamson, R. L., Novascone, S. R., Pastore, G., Spencer, B. W., Stafford, D. S., et al. (2016). *BISON Theory Manual the Equations behind Nuclear Fuel Analysis*. Idaho Falls: Idaho National Laboratory

Hayes, T. A., and Kassner, M. E. (2006). Creep of Zirconium and Zirconium Alloys. *Metallurgical Mater. Trans. A* 37, 2389–2396. doi:10.1007/bf02586213

Hill, R. (1965). A Self-Consistent Mechanics of Composite Materials. *J. Mech. Phys. Sol.* 13, 213–222. doi:10.1016/0022-5096(65)90010-4

Hill, R. (1963). Elastic Properties of Reinforced Solids: Some Theoretical Principles. *J. Mech. Phys. Sol.* 11, 357–372. doi:10.1016/0022-5096(63)90036-x

International Atomic Energy Agency (2006). *Viability of Inert Matrix Fuel in Reducing Plutonium Amounts in Reactors*. IAEA VIENNA.

Jiang, Y. J., Wang, Q. M., and Cui, Y. (2011). Simulation of Irradiation Hardening of Zircaloy within Plate-type Dispersion Nuclear Fuel Elements. *J. Nucl. Mater.* 413 (2), 76–89. doi:10.1016/j.jnucmat.2011.03.021

Kim, Y. S., Jeong, G. Y., Park, J. M., and Robinson, A. B. (2015). Fission Induced Swelling of UMo/Al Dispersion Fuel. *J. Nucl. Mater.* 465, 142–152. doi:10.1016/j.jnucmat.2015.06.006

Lielens, G., Pirotte, P., Couniot, A., Dupret, F., and Keunings, R. (1998). Prediction of Thermomechanical Properties for Compression Moulded Composites. *Compos. Part. A. Appl. Sci. Manuf.* 29, 63–70. doi:10.1016/s1359-835x(97)00039-0

Lipkina, K., Savchenko, A., and Skupov, M. (2014). Metallic Inert Matrix Fuel Concept for Minor Actinides Incineration to Achieve Ultra-high Burn-Up. *J. Nucl. Mater.* 452, 378–381. doi:10.1016/j.jnucmat.2014.04.030

Liu, M. L., Lee, Y. H., and Rao, D. V. (2018). Development of Effective thermal Conductivity Model for Particle-type Nuclear Fuels Randomly Distributed in a Matrix. *J. Nucl. Mater.* 508, 168–180. doi:10.1016/j.jnucmat.2018.05.044

Lombardi, C., Luzzi, L., Padovani, E., and Vettraino, F. (2008). Thoria and Inert Matrix Fuels for a Sustainable Nuclear Power. *Prog. Nucl. Energ.* 50 (8), 944–953. doi:10.1016/j.pnucene.2008.03.006

MacDonald, P. E., and Thompson, L. B. (1978). *MATPRO. A Handbook of Materials Properties for Use in the Analysis of Light Water Reactor Fuel Rod Behavior*. United States: Technical Report.

Mantari, J. L., and Canales, F. G. (2020). Compact and Unified Elasto-Plastic Formulation to Study Isotropic Plates. *Int. J. Non-Linear Mech.* 118, 103253. doi:10.1016/j.ijnonlinmec.2019.103253

Matsuda, T., Ohno, N., Tanaka, H., and Toshihiro, S. (2002). Homogenized In-Plane Elastic-Viscoplastic Behavior of Long Fiber-Reinforced Laminates. *Jsme Int. J.* 45 (4), 538–544. doi:10.1299/jsmea.45.538

Mori, T., and Tanaka, K. (1973). Average Stress in Matrix and Average Elastic Energy of Materials with Misfitting Inclusions. *Acta Met.* 21, 571–574. doi:10.1016/0001-6160(73)90064-3

Neeft, E. A. C., Bakker, K., Schram, R. P. C., Conrad, R., and Koning, R. J. (2003). The EFTTRA-T3 Irradiation experiment on Inert Matrix Fuels. *J. Nucl. Mater.* 320 (1-2), 106–116. doi:10.1016/s0022-3115(03)00176-4

Nemat-Nasser, S. (1999). Averaging Theorems in Finite Deformation Plasticity. *Mech. Mater.* 31, 493–523. doi:10.1016/s0167-6636(98)00073-8

Rest, J. (2004). A Model for Fission-Gas-Bubble Behavior in Amorphous Uranium Silicide Compounds. *J. Nucl. Mater.* 325 (2-3), 107–117. doi:10.1016/j.jnucmat.2003.11.008

Rest, J. (1997). Application of a Mechanistic Model for Radiation-Induced Amorphization and Crystallization of Uranium Silicide to Recrystallization of UO2. *J. Nucl. Mater.* 248, 180–184. doi:10.1016/s0022-3115(97)00117-7

Rest, J. (1995). *The DART Dispersion Analysis Research Tool: A Mechanistic Model for Predicting Fission-Product-Induced Swelling of Aluminum Dispersion Fuels*. Lemont: Argonne National Laboratory

Reuss, A. (1929). Berechnung Der Fliessgrenze Von Mischkristallen Auf Grund der plastizitätsbedingung fürEinkristalle. *Math. Mech.* 9, 49–58. doi:10.1002/zamm.19290090104

Rodriguez, P., Krishnan, R., and Sundaram, C. V. (1984). Radiation Effects in Nuclear Reactor Materials-Correlation with Structure. *Bull. Mater. Sci.* 6 (2), 339–367. doi:10.1007/bf02743907

Samadian, P., Butcher, C., and Michael, J. (2020). New Mean-Field Homogenization Schemes for the Constitutive Modelling of the Elastic and Elastoplastic Deformation Behavior of Multi-phase Materials. *Mater. Today Commun.* 24, 24–100707. doi:10.1016/j.mtcomm.2019.100707

Sanchez-Palencia, E., and Zaoui, A. (1987). "Homogenization Techniques for Composites Media," in *Lecture Notes in Physics 272* (Berlin: Springer-Verlag).

Savchenko, A. M., Vatulin, A. V., Morozov, A. V., and Sirotin, V. L. (2006). Inert Matrix Fuel in Dispersion Type Fuel Elements. *J. Nucl. Mater.* 352 (1-3), 372–377. doi:10.1016/j.jnucmat.2006.03.003

Savchenko, A., Konovalov, L., Vatulin, A., Morozov, A., Orlov, V., Uferov, O., et al. (2007). Dispersion Type Zirconium Matrix Fuels Fabricated by Capillary Impregnation Method. *J. Nucl. Mater.* 362 (2-3), 356–363. doi:10.1016/j.jnucmat.2007.01.211

Savchenko, A. M., Konovalov, I. I., Vatulin, A. V., and Glagovsky, E. M. (2009). New Concept of Designing Pu and MA Containing Fuel for Fast Reactors. *J. Nucl. Mater.* 385 (1), 148–152. doi:10.1016/j.jnucmat.2008.10.035

Semih Perdahcıoglu, E., and Hubert, G. (2011). Constitutive Modeling of Two Phase Materials Using the Mean Field Method for Homogenization. *Int. J. Mater. Forming* 4, 93–102. doi:10.1007/s12289-010-1007-6

Shi, X., Ma, S., Liu, C., and Wu, Q. (2017). Selective Laser Melting-Wire Arc Additive Manufacturing Hybrid Fabrication of Ti-6Al-4V alloy: Microstructure and Mechanical Properties. *Mater. Sci. Eng. A* 684, 196–204. doi:10.1016/j.msea.2016.12.065

Sun, C. T., and Vaidya, R. S. (1996). Prediction of Composite Properties from a Representative Volume Element. *Compos. Sci. Technol.* 56, 171–179. doi:10.1016/0266-3538(95)00141-7

Sun, W., You, F., Kong, F., and Wang, X. (2020). Effect of Residual Stresses on the Mechanical Properties of Ti-TiAl Laminate Composites Fabricated by Hot-Pack Rolling. *Mater. Characterization* 166, 110394. doi:10.1016/j.matchar.2020.110394

Suzuki, H. S. M. (2005). *Light Water Reactor Fuel Analysis Code FEMAXI-6 (Ver.1).*

Vatulin, A. V., Stetsky, Y. A., Trifonov, Y. I., and Khotyashov, G. I. (2001). Composite Materials and Systems as Alternative Inert Matrix Fuel to Dispose Civil or Weapon Grade Plutonium in Light Water Reactors. *Prog. Nucl. Energ.* 38 (3-4), 321–326. doi:10.1016/s0149-1970(00)00126-8

Voigt, W. (1889). Über die Beziehung zwischen den beiden Elastizitätskonstanten isotroper Körper. *Wied. Ann. Phys.* 38, 573–587. doi:10.1002/andp.18892741206

Wang, Q. M., Cui, Y., Ding, S. R., and Huo, Y. Z. (2011). Simulation of the Coupling Behaviors of Particle and Matrix Irradiation Swelling and Cladding Irradiation Growth of Plate-type Dispersion Nuclear Fuel Elements. *Mech. Mater.* 43 (4), 222–241. doi:10.1016/j.mechmat.2011.01.004

Wang, Q. M., Yan, X. Q., Ding, S. R., and Huo, Y. Z. (2010). Research on the Interfacial Behaviors of Plate-type Dispersion Nuclear Fuel Elements. *J. Nucl. Mater.* 399 (1), 41–54. doi:10.1016/j.jnucmat.2010.01.001

Wu, L., Doghri, I., and Noels, L. (2015). An Incremental-Secant Mean-Field Homogenization Method with Second Statistical Moments for Elasto-Plastic Composite Materials. *Philos. Mag. Abingdon (Abingdon)* 114, 1–36. doi:10.1080/14786435.2015.1087653

Zhang, J., and Ding, S. (2020). Mesoscale Simulation Research on the Homogenized Elasto-Plastic Behavior of FeCrAl Alloys. *Mater. Today Commun.* 22, 100718. doi:10.1016/j.mtcomm.2019.100718

Zhang, J., Wang, H., Wei, H., Zhang, J., Tang, C., Lu, C., et al. (2021). Modelling of Effective Irradiation Swelling for Inert Matrix Fuels. *Nucl. Eng. Tech.* doi:10.1016/j.net.2021.02.019

Zhao, Y., Gong, X., Cui, Y., and Ding, S. (2016). Simulation of the Fission-Induced Swelling and Creep in the CERCER Fuel Pellets. *Mater. Des.* 89, 183–195. doi:10.1016/j.matdes.2015.09.135

Zhao, Y. M., Gong, X., Ding, S. R., and Huo, Y. Z. (2014). A Numerical Method for Simulating the Non-homogeneous Irradiation Effects in Full-Sized Dispersion Nuclear Fuel Plates. *Int. J. Mech. Sci.* 81, 174–183. doi:10.1016/j.ijmecsci.2014.02.012

**Conflict of Interest:** The authors declare that the research was conducted in the absence of any commercial or financial relationships that could be construed as a potential conflict of interest.